# Femtosecond laser impact on calcium phosphate bioceramics assessed by micro-Raman spectroscopy and osteoblastic behaviour

Marie Lasgorceix, Liliana Grenho, Maria Helena Fernandes, Cédric Ott, Laurent Boilet, Anne Leriche, Fernando Monteiro, Francis Cambier, Stéphane Hocquet

Journal of the European Ceramic Society 38 (2018) 5545–5553

Contents lists available at ScienceDirect

Journal of the European Ceramic Society

journal homepage: www.elsevier.com/locate/jeurceramsoc

Original Article

# Femtosecond laser impact on calcium phosphate bioceramics assessed by micro-Raman spectroscopy and osteoblastic behaviour

Marie Lasgorceix[a,*], Liliana Grenho[b], Maria Helena Fernandes[b], Cédric Ott[a], Laurent Boilet[a], Anne Leriche[c], Fernando Monteiro[d], Francis Cambier[a], Stéphane Hocquet[a]

[a] Belgian Ceramic Research Centre, Member of EMRA, Avenue Gouverneur Cornez, 4, B-7000 Mons, Belgium
[b] LAQV/REQUINTE, U. Porto, Portugal
[c] LMCPA-UVHC, Pôle Universitaire de Maubeuge, Boulevard Charles de Gaulle, 59600 Maubeuge, France
[d] INEB, Universidade do Porto, Rua do Campo Alegre, 823, 4150-180 Porto, Portugal

ARTICLE INFO

*Keywords:*
Calcium phosphate bioceramics
Laser micropatterning
Micro-Raman spectroscopy
Phase transformation
Osteoblastic behaviour

ABSTRACT

The present work is an investigation of the biological response to the presence of grooves 3 μm deep, 15 μm wide and spaced by 100 μm, produced with femtosecond laser on β-tricalcium phosphate (β-TCP). The heat affected zone generated by the laser irradiation was investigated. Micro-Raman spectroscopy showed a transformation from β-TCP phase into α-TCP phase, localised inside the grooves. The X Ray Diffraction analyses, correlated with micro-Raman data, confirmed that the use of femtosecond pulsed laser enables to limit the thermal impact. A selection of optimised process parameters allowed to obtain β-TCP micro-patterned surfaces avoiding any phase transformation. The increase of the wettability with the micro-patterning, compared to smooth surfaces, was highlighted. An improvement of the osteoblastic proliferation was also demonstrated. Finally, the tendency of cell elongation along the grooves direction showed the ability of osteoblastic cells to adapt their morphology to the support topography on which they grow.

## 1. Introduction

Today, the development of synthetic bone substitutes is mainly conducted according two ways: by mimicking the chemical composition of the bone mineral part with calcium phosphate (CaP) material [1,2] and by creating controlled porous architectures [3] including interconnected macropores (> 300 μm), necessary to the natural phenomenon of osteoconduction and favouring the processes of biomineralisation and vascularisation. Beta tricalcium phosphate (β-TCP) is a biodegradable ceramic widely used in bone tissue engineering because of its chemical composition ($Ca_3(PO_4)_2$) close to the one of the bone mineral part and its ability to dissolve in physiological media [4]. These chemical properties, associated with an interconnected porous structure, ensure the re-colonization and the replacement of the implant by newly formed bone tissues, during implantation. Plenty studies are focusing on mimicking the bone macroporous structure, by several ways including traditional methods giving rise to random structures, like ceramic slurry impregnation of polymer skeletons [5] or ice templating [6], and new 3D additive manufacturing technologies allowing to obtain controlled and more complex architectures [7]. Because of the development of such various shaping methods, the influence of macroporous architecture has been highlighted in several works [8–10]. Significant differences of biological behaviour observed between several types of implants should be explained not only by the macropourous architectures but also by the surface topography. This specific effect of surface topography, deeply studied by several authors on different materials [11–13] including bioceramics [14], requires more analysis in the case of calcium phosphate materials. The investigation of the influence of surface topography on cell response requires to develop methods to machine the material surfaces without polluting them and without modifying the material chemical composition or crystalline structure. Finally, the effect of surface micro-patterning with few micrometres depth could be hidden by the effect of open microporosity (micropores < 20 μm), which is still not well understood [15]. Consequently, studying the influence of the topography requires working on dense model substrates.

Machining can be carried out by several traditional ways, often leading to residues. By comparison, non-contact laser technology reduces the presence of residual elements and can ensure a high precision in the surface patterning of dense ceramic surfaces. The effect of surface roughness on the cell adhesion has been studied extensively on metal surfaces patterned with a laser. Several evaluations have shown a better

* Corresponding author.
*E-mail address:* m.lasgorceix@bcrc.be (M. Lasgorceix).

https://doi.org/10.1016/j.jeurceramsoc.2018.07.048
Received 22 May 2018; Received in revised form 23 July 2018; Accepted 30 July 2018
Available online 31 July 2018

bone apposition on rough surfaces than smooth surfaces. In particular, the influence of surface topography on cell proliferation, differentiation of osteoblast and bone tissue formation has been reported on titanium surfaces [16]. Several works dealing with laser micropatterning of silicon-based surfaces [17], metallic surfaces [16,18–20] or even zirconia surfaces [14] can be found in literature. In contrast, there is a lack of data concerning the behaviour of laser patterned CaP surfaces because of unwanted phase transformations. Indeed, an allotropic transformation can especially occur in the case of β-TCP laser machining, caused by a heating above the transition temperature comprised between 1125 °C and 1200 °C [21,22], due to the interaction between the laser and the material. Furthermore, the allotropic transformation from the rhombohedral structure of β-TCP to the monoclinic structure of α –TCP causes an increase of the crystal lattice volume about 7% [23], likely to generate microcracks in the material. This transformation also generates an increase of the solubility value from 0.15 mg $L^{-1}$ to 0.24 mg $L^{-1}$ at 37 °C [22], likely to induce changes in calcium and phosphate ion concentrations in the culture media during the in vitro biological evaluation. It is thus necessary to obtain textured substrates without α-TCP, so that the results obtained with the textured substrates can be compared to the results obtained on smooth β-TCP substrates. As shown in a previous study, laser machining should be an interesting way to pattern the CaP surfaces if reducing the heat affected zone by using optimized process parameters [24]. The influence of the laser process parameters on the production of linear grooves on β-TCP surfaces was reported in this previous work. In particular, the effects of the laser power, the pulse frequency, the scan speed and the overlap value, on the definition of the grooves and the amount of unwanted α-TCP phase created during laser treatment, were highlighted. In this previous work, only overall micro-patterned surfaces assessment was conducted by X Ray Diffraction (XRD) analyses. The α-TCP phase was supposed to be located only within the grooves created by the laser, because the α-TCP content, evaluated by XRD on the whole treated surfaces, was correlated with the increase of the grooves width. However, the validation of the laser micro-patterning technique requires a more in-depth analysis of the spatial distribution of the area affected by the laser irradiation allowing to localise exactly the phase transformation. In the present work, we propose to localise precisely the α-TCP phase by micro-Raman spectroscopy and to verify the absence of α-TCP in the case of optimised process parameters in order to produce model β-TCP substrates with and without micro-patterning with identical physico-chemical properties for biological evaluation.

In this context, the present work aimed to perform precise micro-patterning on β-TCP dense surfaces with femtosecond laser technique, to define the heat affected zone by analysing the local phase transformations with micro-Raman spectroscopy and to compare the behaviour of osseous cells seeded on β-TCP smooth or patterned surfaces.

## 2. Materials and methods

### 2.1. Material preparation

#### 2.1.1. Powder synthesis and substrates processing

A β-TCP powder was synthetized by aqueous precipitation, using diammonium phosphate and calcium nitrate solutions [25,26]. Raw powder was then heat treated at 850 °C, ball milled in water during 3 h, and dried at 100 °C after filtering. Pellets (12.5 mm diameter) were produced by uniaxial pressing at 55 MPa followed by sintering at 1100 °C for a dwell time of 2 h (5 °C $min^{-1}$). Sintered pellets were then polished with SiC paper discs and diamond pastes (down to 0.5–3.0 μm) in order to obtain reproducible smooth surfaces.

#### 2.1.2. Laser treatment

Grooves were produced on the dense β-TCP polished surfaces with a femtosecond pulsed laser, at 1030 nm wavelength with 270 fs pulse width.

For XRD analyses, grooves were produced on the whole β-TCP surfaces, with a hatch (distance between 2 lines) fixed at 20 μm. For local micro-Raman analyses, single grooves were produced in order to evaluate the heat affected zone around the grooves.

According to the results observed in a previous study [24], in order to localise the phase transformation and even to precisely evaluate the thermal impact of the laser on the material, the three following combinations of laser treatments were considered:

- 7.0 W, 500 kHz, 200 mm/s (overlap 97%);
- 2.0 W, 500 kHz, 200 mm/s (overlap 97%);
- 7.0 W, 250 kHz, 3000 mm/s (overlap 21%).

Process parameters (pulse frequency, scan speed and laser power) were then chosen in order to produce micro-patterning without phase transformation for the substrates dedicated to the biological assays and wettability evaluation. Linear micro-patterns were produced on the whole surface with a hatch fixed at 100 μm.

### 2.2. Material characterisation

#### 2.2.1. Physico-chemical characterisation

The crystalline phases of powder and ceramic substrates, before and after laser treatment, were determined using X-ray diffraction (XRD) on whole treated surfaces. XRD data were collected using CuKα radiation on θ/2θ diffractometers (Bruker model D8). The identification of crystalline phases was achieved with EVA software® by comparing the diffraction patterns with International Centre for Diffraction Data–Powder Diffraction Files (ICDD-PDF).

Raman spectroscopy was used to precisely localise the phase transformations induced by the laser treatment. Micro-Raman spectra were recorded on the β-TCP surfaces patterned with single grooves, using a Senterra (Bruker) instrument with 532 nm laser wavelength, connected to a microscope with 50× magnification, giving rise to a 2 μm spot diameter. The analyses were locally performed on grooves bottom, on the grooves walls, on the border of the grooves and on the untreated areas located 5 μm far from the grooves. Micro-Raman spectra were also recorded on β-TCP untreated surfaces in order to provide a reference spectrum for the initial β-TCP material.

#### 2.2.2. Surface analyses

The surface topography of the ceramic substrates, before and after laser treatment, was observed and analysed by Confocal Laser Scanning Microscopy (CLSM) (Keyence VK-X250) with a standard resolution 1024 × 768. The dimensional parameters (grooves width and depth) of the patterned surfaces were evaluated from observations performed on three samples. Linear roughness Ra was also evaluated on the grooves and on the surface between grooves, by confocal microscopy (Keyence VK-X250) on triplicates, by stitching 48 pictures obtained with a 150x magnification lens and a 0.08 μm vertical pitch. The analysing conditions for establishment of the Ra parameter were chosen according to ISO4288:96 (evaluation length 4 mm and CutOff 0.8 mm, giving 5 sampling lengths).

#### 2.2.3. Wettability

Water contact angle measurements (Dataphysics contact angle system OCA) were performed on the β-TCP substrates, as-sintered, polished and patterned by femtosecond laser irradiation. Values were recorded every 2 s during 5 min of the droplet spreading. Assays were reproduced on 5 samples of each type. Values were averaged over all the experiment duration and 5 samples.

### 2.3. In vitro evaluation: osteoblastic behaviour

#### 2.3.1. Cell culture and materials seeding

MG63 osteoblastic cells (ATCC number CRL-1427™) were cultured

until 70–80 % confluence in α-Minimal Essential Medium (α–MEM), with 10% fetal bovine serum, 100 IU/mL penicillin, 100 µg/mL streptomycin and 2.5 µg/mL amphotericin B (all from Gibco), at 37 °C and 5% $CO_2$/air. For sub-culturing, the cell layer was detached with trypsin–EDTA solution (0.05% trypsin, 0.25% EDTA; 5 min at 37 °C, both from Sigma-Aldrich).

Prior to cell seeding, β-TCP substrates were sterilized by autoclaving 20 min at 125 °C. MG63 cells ($2 \times 10^4$ cells/cm$^2$) were seeded over the smooth and the linear patterned β-TCP substrates (placed on 24-well culture plates). Seeded materials were cultured for periods up to 7 days. In parallel, cells were cultured on standard polystyrene cell culture plates, as a control of the performance of the cell culture system. Cell response was evaluated on triplicates for metabolic activity and cell morphology observation under Scanning Electron Microscopy (SEM) and CLSM.

*2.3.2. Cellular behaviour*

*2.3.2.1. Metabolic activity*. The resazurin assay was used to estimate the cell metabolic activity. In this assay, a nontoxic alamar blue dye (resazurin) is reduced by intracellular enzyme activity to resorfin, a fluorescent form of alamar blue.

After 1, 3 and 7 days in culture, the medium was carefully removed from the wells, the substrates were transferred to new wells, and fresh media with 10% (v/v) of resazurin solution was added to each well. Samples were then incubated for 3 h at 37 °C in humidified atmosphere (95% air/5% $CO_2$). The fluorescence intensity was measured in a microplate reader (Synergy HT, Biotek) at 530 and 590 nm for excitation and emission wavelength, respectively. In addition, a parallel experiment was run in which the samples were incubated in culture medium (without cell seeding), using the same protocol as the cell cultures, to compensate for the background reduction. Results were expressed as Fluorescence/cm$^2$.

*2.3.2.2. SEM and CLSM observation*. For SEM analyses, substrates were washed twice in phosphate buffered saline (PBS, Sigma-Aldrich) and fixed with 1.5% glutaraldehyde in sodium cacodylate buffer (pH 7.3, 10 min, both from Sigma-Aldrich). Then the fixed samples were dehydrated in sequential graded ethanol solutions (70%–100%), critical point dried (CPD 7501, Polaron Range) and sputter coated with gold. The sputtered samples were then analysed by SEM (FEI Quanta 400FEG ESEM/EDAX Genesis X4M).

For CLSM assessment, samples were fixed with 3.7% paraformaldehyde for 15 min. Cell cytoskeleton filamentous actin (F-actin) was visualised by treating the cells with Alexa Fluor 488-conjugated phalloidin (1:100, Molecular Probes) for 1 h. A counterstaining with propidium iodide (1 mg/mL, BD Biosciences) for 10 min was used for cell nuclei labelling. Finally, labelled substrates were examined by confocal microscopy (Leica TCS SP5 AOBS instrument, Leica).

To determine cell area and elongation, four different areas of each sample were analysed using the ImageJ software.

*2.3.2.3. Statistics and data analysis*. Quantitative data are presented as mean ± standard deviation of three replica of each type of material samples. Significant differences in statistical analysis were determined using one-way ANOVA test. A p value less than 0.05 was considered to be statistically significant.

## 3. Results and discussion

### 3.1. Heat affected zone analysis

The XRD analyses of the whole treated β-TCP surfaces and the local micro-Raman analyses performed on single grooves are presented in Figs. 1 and 2 respectively. Micro-Raman spectra were recorded between 900 and 1200 cm$^{-1}$, this range being the more relevant to differentiate the α and β phases of TCP.

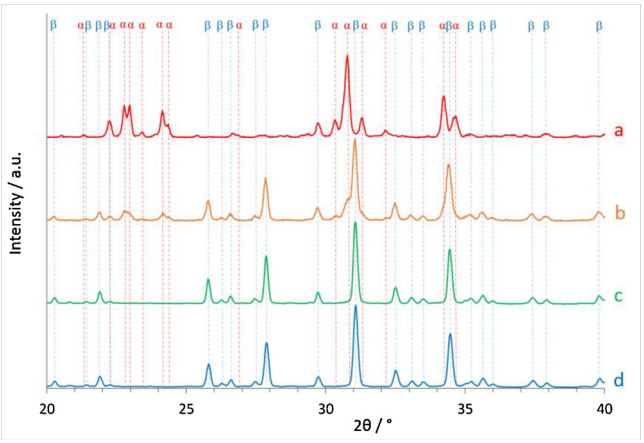


**Fig. 1.** X-ray diffraction patterns of β-TCP surfaces treated by laser irradiation at 7 W, 500 kHz, 200 mm/s (a); at 2 W, 500 kHz, 200 mm/s (b); at 7.0 W, 250 kHz, 3000 mm/s (c) and untreated (d) for β-TCP reference; β-TCP phase notified with blue β symbol; α-TCP phase notified with red α symbol. (For interpretation of the references to colour in this figure legend, the reader is referred to the web version of this article).

XRD analyses performed on the whole treated surfaces with non-optimized laser parameters (7 W, 500 kHz, 200 mm/s), i.e with high laser power and high overlap value (97%), show the presence of high amount of α-TCP phase (> 90%) (Fig. 1a). Micro-Raman analyses confirm the majority presence of α-TCP inside the grooves. More particularly, this unwanted phase is the main phase detected in the bottom (Fig. 2a, red curve), on the walls (Fig. 2a, orange curve) and on the border of the grooves (Fig. 2a, green curve), with a single band at 965.0 cm$^{-1}$ attributed to vibration mode $\nu_1$ of the phosphate groups of α-TCP (Table 1) [27,28]. Whereas spectra obtained on the untreated areas, even near the grooves (5 µm from the border of the groove; Fig. 2a, blue curve), attest the presence of β-TCP with two lines at 969.5 and 949.0 cm$^{-1}$ specific of bands attributed to vibration mode $\nu_1$ of the phosphate groups of β –TCP (Table 1) [27,29]. These analyses suggest a local phase transformation thus confirming the highly localised heating produced by the femtosecond laser irradiation, allowing to suppose that the use of femtosecond pulsed laser enables to limit the heat affected zone as expected.

In the case of surfaces treated with a lower laser power (2 W, 500 kHz, 200 mm/s) and with the same overlap value (97%), the two phases β-TCP and α-TCP are detected by XRD on the whole treated surfaces (Fig. 1b). Micro-Raman analyses, performed locally near and inside the single groove, confirm the presence of both phases inside the groove. This result is highlighted by the shift of the theoretical bands attributed to the vibration mode $\nu_1$ of the phosphate groups of β –TCP at 969.5 cm$^{-1}$ and 949.0 cm$^{-1}$ towards respectively 968.0 cm$^{-1}$ and 950.5 cm$^{-1}$ on the grooves walls (Fig. 2b, orange curve) and until 967.5 cm$^{-1}$ and 955.0 cm$^{-1}$ in the grooves bottom (Fig. 2b, red curve). These two bands, specific of β-TCP, are thus tending towards a single band at 965.0 cm$^{-1}$ attributed to vibration mode $\nu_1$ of the phosphate groups of α-TCP. On the contrary, spectra obtained from Raman measurements performed near the groove (Fig. 2b, blue curve) and even on the border of the groove (Fig. 2b, green curve) are similar to the spectrum obtained on the untreated β-TCP surfaces (Fig. 2b, black curve) showing that areas around the laser pass are spared by the thermal impact. A reduction of the laser power leads thus to a limitation of the phase transformation β-TCP towards α-TCP, while still allowing grooving, since the unwanted phase α-TCP is no longer the majority phase inside the grooves as it is the case with high powerful treatments. Moreover, the thermal diffusion on the substrate surface is limited by the decrease of the laser power because the spectra obtained at a distance of 5 µm from the groove (Fig. 2b, blue curve) and even on the border of the groove (Fig. 2b, green curve) are characteristic spectra of

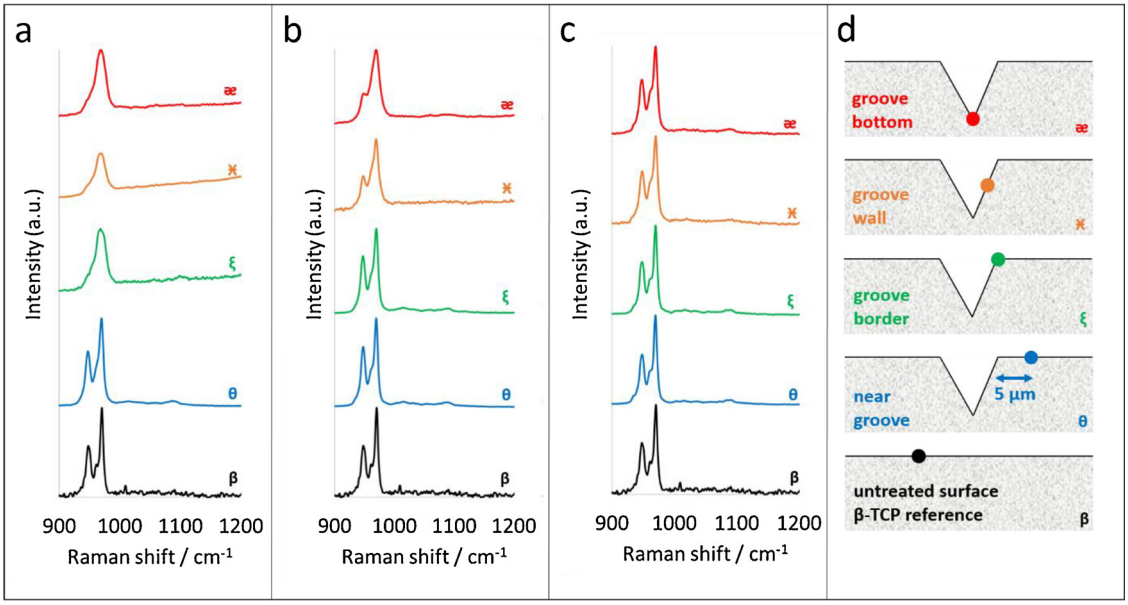


**Fig. 2.** Micro-Raman spectra of β-TCP untreated surfaces (black curve, β symbol) and β-TCP surfaces treated with femtosecond laser (coloured curves) in the following conditions : a) 7.0 W, 500 kHz, 200 mm/s, overlap 97%; b) 2.0 W, 500 kHz, 200 mm/s, overlap 97%; c) 7.0 W, 250 kHz, 3000 mm/s, overlap 21%; d) schematic sectional view of the grooves and location of micro-Raman measurements materialised by coloured dots corresponding to the spectra: red spectra (æ symbol) recorded in the bottom of the grooves; orange spectra (Ж symbol) recorded on the walls of the grooves; green spectra (ξ symbol) recorded on the border of the grooves; blue spectra (θ symbol) recorded on the untreated area, 5 µm from the grooves. (For interpretation of the references to colour in this figure legend, the reader is referred to the web version of this article).

the β-TCP phase. These results confirm again the localized heating produced by the femtosecond laser and that the adaptation of the laser parameters can contribute to reduce the local thermal impact.

After optimization of the laser conditions [24], no α-TCP is detected neither by XRD on the whole treated surfaces (Fig. 1c) nor by local micro-Raman analyses inside single groove (Fig. 2c). Indeed, both characterisation methods highlight the presence of β-TCP with similar diffractograms and Raman spectra on untreated and laser treated areas. This result allows to validate the optimisation of the laser conditions in order to obtain β-TCP samples with micro-patterning and without secondary phase.

Consequently, both XRD and micro-Raman methods confirmed that the process optimisation permitted to produce β-TCP patterned substrates for biological evaluation allowing to observe the effects of surface topography on cell behaviour avoiding the effects of the material properties related to changes of crystal structure.

### 3.2. Surface analysis

Representative pictures of the confocal observations performed on the β-TCP surfaces, patterned with the optimal process parameters (7.0 W, 250 kHz, 3000 mm/s, overlap 21%) and a hatch of 100 µm, are given in Fig. 3.

The linear roughness parameter Ra, evaluated in triplicates, is significantly higher inside the grooves (0.898 ± 0.013 µm) than on the untreated areas between two grooves (0.014 ± 0.001 µm). Concerning the grooves dimensions, the depth was estimated, on 3 multiline profiles (Fig. 3c), at 2.68 ± 0.07 µm and the width at 15.31 ± 0.64 µm. These values voluntarily guarantee cavities too narrow to allow the MG63 osteoblastic cells to undergo a gravity effect since they are too large (20–30 µm) to fall down in the bottom of the grooves. This design might therefore make it possible to clearly identify the topographic effect on cellular behaviour.

**Table 1**
Wavenumber ($cm^{-1}$) and assignment of the Raman bands observed on the spectra recorded over the range 900–1200 $cm^{-1}$ in the grooves bottom, on the grooves walls, on the grooves border and on the surface near the grooves for each laser treatment, and on the untreated β –TCP surfaces for reference [27,28]. (For interpretation of the references to colour in this Table legend, the reader is referred to the web version of this article).

| Laser treatment | Localization | Bands Wavenumber ($cm^{-1}$) | Assignment (vibrational mode and phase) |
|---|---|---|---|
| 7.0 W, 500 kHz 200 mm/s overlap 97 % | Groove bottom | 965 | Vibration mode $\nu_1$ of $PO_4^{3-}$ of α-TCP |
| | Groove wall | 965 | Vibration mode $\nu_1$ of $PO_4^{3-}$ of α-TCP |
| | Groove border | 965 | Vibration mode $\nu_1$ of $PO_4^{3-}$ of α-TCP |
| | Surface near groove | 969.5 - 949.0 | Vibration mode $\nu_1$ of $PO_4^{3-}$ of β –TCP |
| 2.0 W, 500 kHz 200 mm/s overlap 97 % | Groove bottom | 967.5 - 955.0 | Shift towards $\nu_1$ $PO_4^{3-}$ of α-TCP |
| | Groove wall | 968.0 - 950.5 | Shift towards $\nu_1$ $PO_4^{3-}$ of α-TCP |
| | Groove border | 969.5 - 949.0 | Vibration mode $\nu_1$ of $PO_4^{3-}$ of β –TCP |
| | Surface near groove | 969.5 - 949.0 | Vibration mode $\nu_1$ of $PO_4^{3-}$ of β –TCP |
| 7.0 W, 250 kHz 3000 mm/s overlap 21 % | Groove bottom | 969.5 - 949.0 | Vibration mode $\nu_1$ of $PO_4^{3-}$ of β –TCP |
| | Groove wall | 969.5 - 949.0 | Vibration mode $\nu_1$ of $PO_4^{3-}$ of β –TCP |
| | Groove border | 969.5 - 949.0 | Vibration mode $\nu_1$ of $PO_4^{3-}$ of β –TCP |
| | Surface near groove | 969.5 - 949.0 | Vibration mode $\nu_1$ of $PO_4^{3-}$ of β –TCP |
| None | Random | 969.5 - 949.0 | Vibration mode $\nu_1$ of $PO_4^{3-}$ of β –TCP |

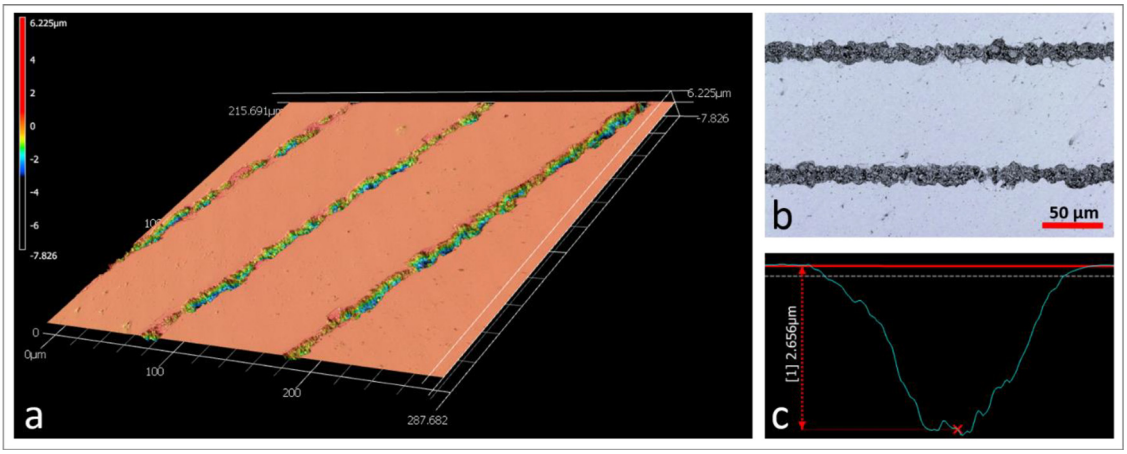


**Fig. 3.** Observation by confocal microscopy of the patterned β-TCP surface: a) three dimensional view; b) top view; c) groove profile.

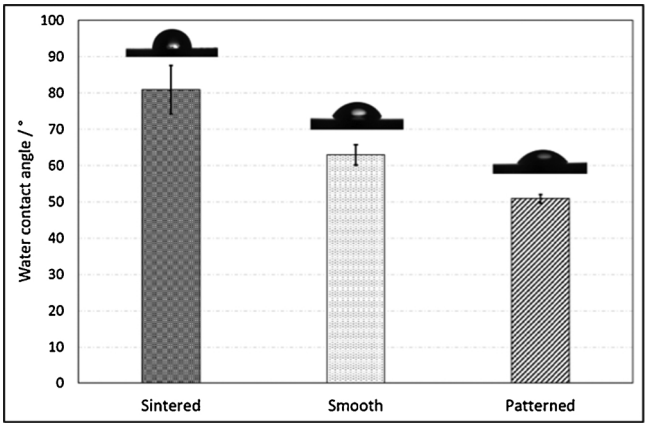


**Fig. 4.** Water contact angle measurements on β-TCP substrates, as-sintered, polished (smooth) and patterned by femtosecond laser irradiation.

The distance between two grooves, evaluated on triplicates at 100.01 ± 0.03 µm, is really close to the 100.00 µm expected. This distance, higher than the MG63 osteoblastic cell size (20–30 µm), ensures the discontinuity between two cell lines that may possibly be formed along the grooves. Thus, this accurate design makes possible to evaluate the behaviour of cells touching the grooves and cells on areas between two grooves, without any contact with them. The interest of this configuration is to see if the behaviour of the cells, without contact with the grooves, can be modified only thanks to the interactions with the cells themselves in contact with the grooves.

### 3.3. Wettability

The water contact angle values measured on β-TCP substrates, as-sintered, polished (smooth) and patterned by femtosecond laser irradiation (7.0 W, 250 kHz, 3000 mm/s, overlap 21%, hatch 100 µm), are given in Fig. 4.

A previous study had shown a better wettability of laser-patterned

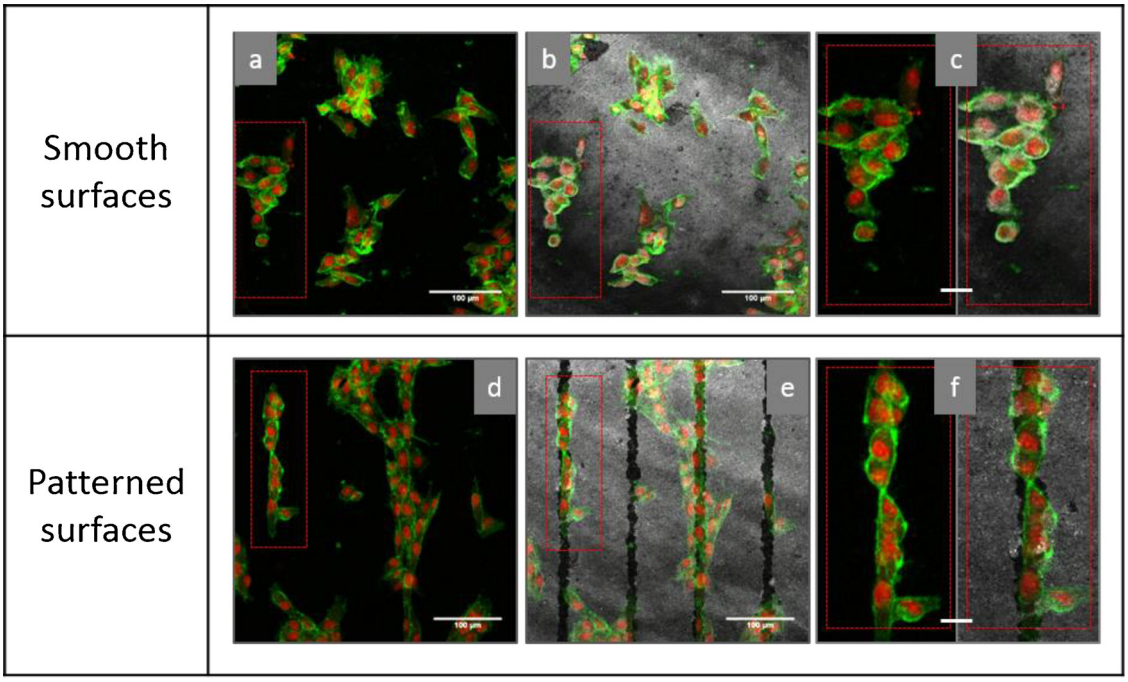


**Fig. 5.** Observation by CLSM of MG63 osteoblastic cells adhering on β-TCP substrates, one day after seeding (cytoskeleton stained in green, nucleus stained in red); a), b) and c) smooth surfaces, d), e) and f) patterned surfaces; scale bar 100 µm (a, b, d, e) and 25 µm (c, f). (For interpretation of the references to colour in this figure legend, the reader is referred to the web version of this article).

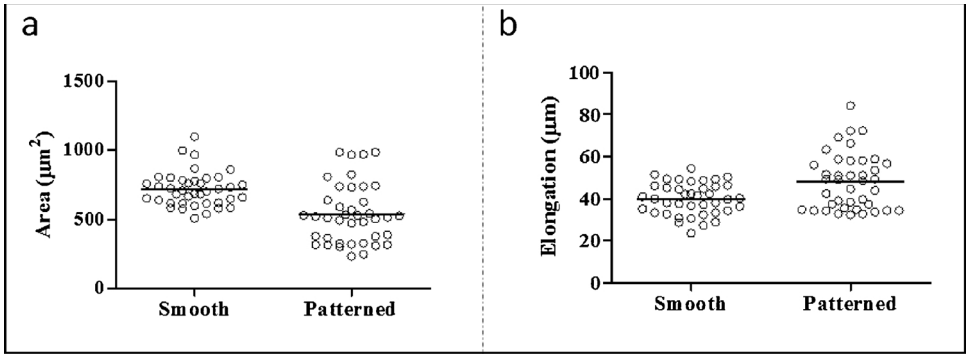


**Fig. 6.** Quantification of cell area (a) and cell elongation (b) of MG63 cells cultured for 24 h on β-TCP smooth and patterned surfaces.

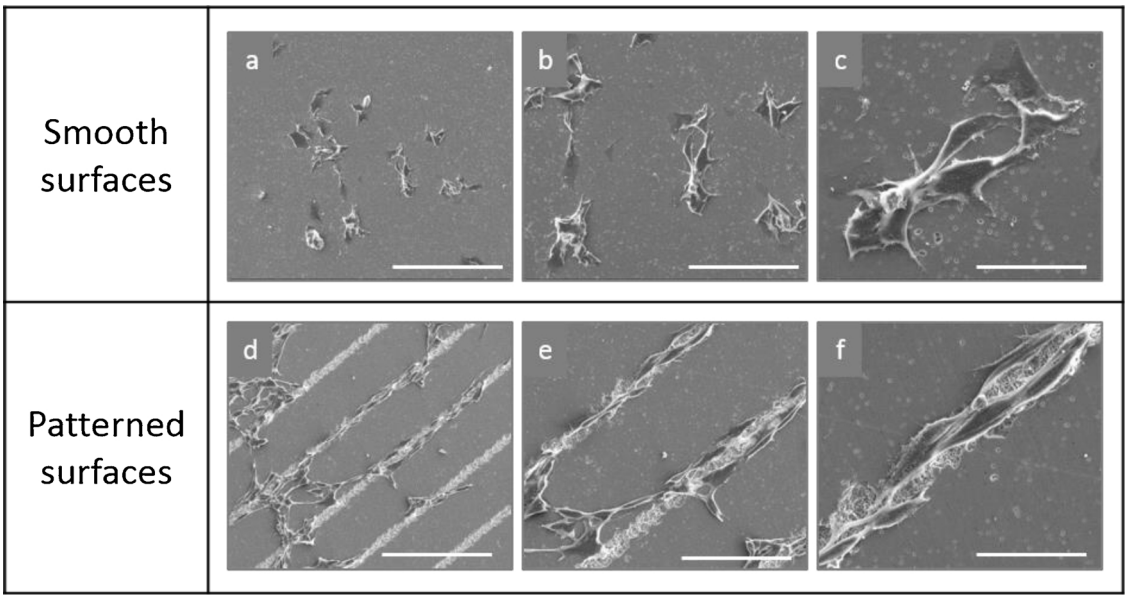


**Fig. 7.** SEM micrographs of MG63 osteoblastic cells adhering on sintered β-TCP substrates, one day after seeding: smooth surfaces (a–c) and patterned surfaces (d–f); scale bar: 200 µm (a, d), 100 µm (b, e) and 40 µm (c, f).

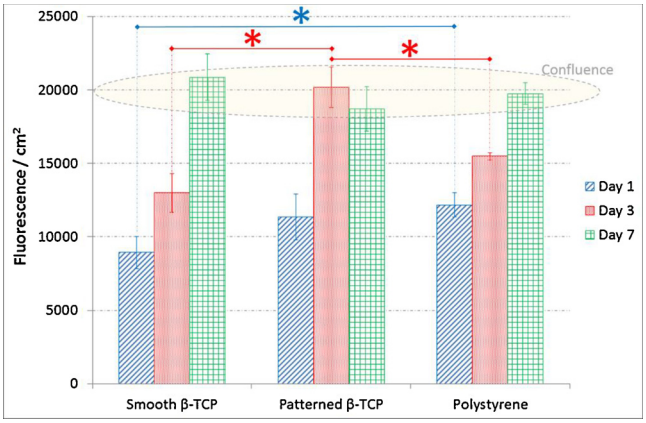


**Fig. 8.** Evolution of MG63 cell density (values reported to the area of the culture substrate) throughout the culture time. A p value (from one-way ANOVA test) less than 0.05, identified with * symbol, was considered to be statistically significant.

substrates compared to as-sintered and smooth surfaces, in the case of linear grooves spaced 20 µm apart [24]. In the present study, lower contact angle values are still obtained in the case of patterned surfaces with grooves spaced 100 µm apart, compared to as-sintered and smooth surfaces (Fig. 4). The contact angles obtained either for smooth or patterned surfaces are within the range frequently described as optimal for biomaterials to attain ideal levels of cell attachment and spreading [30]. The wetting behaviour modification can be attributed to an effect of capillarity due to the presence of grooves. The contact angle can also be affected by the difference in roughness values between the grooves (Ra = 0.898 µm) and the smooth areas between grooves (Ra = 0.014 µm) [31]. Finally, a visual observation during the droplet spreading highlighted a slight wetting anisotropy, from circular shape to elliptic shape, which can be governed by the topographic linear design, as it has been described in literature with micro-wrinkled surfaces [32].

### 3.4. Osteoblastic behaviour

Osteoblastic behaviour was investigated on β-TCP substrates, polished (smooth) and patterned by femtosecond laser irradiation (7.0 W, 250 kHz, 3000 mm/s, overlap 21%, hatch 100 µm).

#### 3.4.1. Cell attachment, morphology and orientation

The cell attachment, morphology and distribution on the smooth and patterned surfaces were analysed by CLSM and SEM observation.

Fig. 5 presents representative CLSM images of the colonized materials at day 1. On the smooth substrates, cells are randomly dispersed (Fig. 5a–c), whereas in the case of patterned surfaces they fill

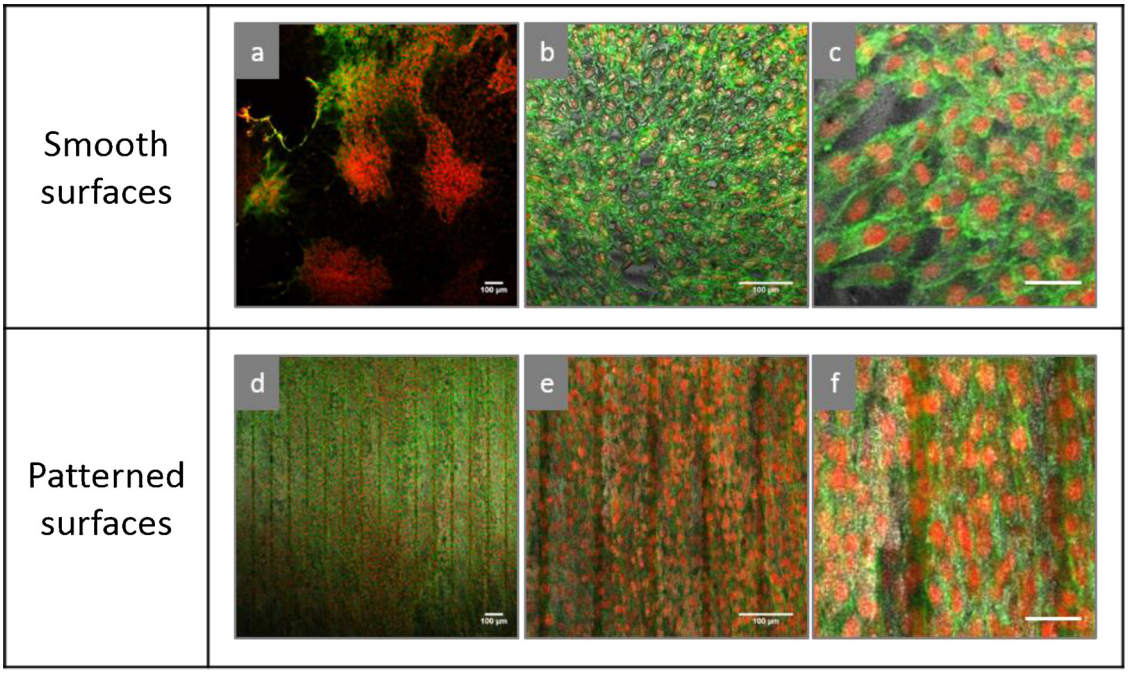


**Fig. 9.** Observation by CLSM of MG63 osteoblastic cells adhering on β-TCP substrates, three days after seeding (cytoskeleton stained in green, nucleus stained in red); a)–c) smooth surfaces, d)–f) patterned surfaces; scale bar 100 μm (a, b, d, e) and 50 μm (c, f). (For interpretation of the references to colour in this figure legend, the reader is referred to the web version of this article).

preferentially the grooves created by the laser (Fig. 5d–f). On these surfaces, high magnification images confirm that cells attach especially on the grooves and seem to be aligned along the grooves direction (Fig. 5e, f). The grooves cause a conditioning to the cell attachment but do not completely restrict the subsequent cell spreading. Thus, although cells tend to show an elongated appearance, some cells spread towards the surface between the grooves presenting a more rounded appearance (Fig. 5d–f). This is because the depth and the width of the grooves are smaller than the cells normal dimensions. This surface topography has an additional feature, i.e. the distance between the grooves seem to favour the expansion of the cytoplasm towards to the neighbouring groove (Fig. 5d, e). These cell extensions reflect the cytoskeleton dynamics during the cell adhesion process and have a role in substrate probing collecting spatial, topographic and chemical information [33]. In the patterned surface this behaviour appears to favour cell bridging between grooves (Fig. 5d, e). This phenomenon is highly favourable to the formation of continuous cell layers. The results indicate that the cell organization on the patterned substrate, which totally contrasts with the cell clusters observed in the case of smooth surfaces (Fig. 5a–c), is favourable to the cell migration phenomenon and thus to the cell colonisation. The localisation of cells on the grooves cannot be explained by gravity effects as it is the case for macro-architectures [34]. Indeed, in the present case, as mentioned above, the depth and the width of the grooves are smaller than the cells dimensions, allowing to identify exclusively the surface effects.

The effect of surface topography on cell morphology is further confirmed through cell area and cell elongation quantification (Fig. 6). The cells cultured on patterned surface show a slightly smaller cell area and higher cell elongation as compared to cells cultured on smooth surface. Although differences are not statistically significant, the patterned surface show a higher level of results dispersion, which is expected as the cells have to adapt to rough and smooth topographies.

The SEM observations made at day 1 confirm the CLSM observations regarding cell attachment, morphology and orientation on the two surfaces (Fig. 7). On the patterned ceramic, the tendency of elongation is clearly visible along the grooves showing that cells have the ability to adapt their morphology to follow the topographic design. Cell bridging is also noticed.

*3.4.2. Metabolic activity/cell proliferation*

The metabolic activity was assessed by the rezasurin assay, which provides information on the density of viable and metabolic active cells present in the culture substrate. Thus, the observed values throughout the culture time provide indirect information on the number of such cells.

Fig. 8 shows that the metabolic activity of cells throughout the 7-day culture time, reported towards the area of the substrate surface, increases steadily with the culture time on control (standard polystyrene culture plates) and ceramic surfaces.

Compared to the control, on the ceramic smooth surfaces, values are significantly lower at day 1 (27%, $p < 0.02$), reflecting a lower number of attached metabolic active cells. At day 3, cell density of viable cells is still slightly lower (16%) but not so significantly ($p < 0.11$). Afterwards, cell growth rate increases and, at day 7, cell density on smooth surfaces is similar to that on control cultures.

The patterned surfaces exhibit a totally different behaviour. Compared to the smooth surfaces, cell density appears higher at day 1 (27%, $p = 0.09$) and is significantly higher at day 3 (55%, $p = 0.03$). Indeed, cell growth rate on patterned surfaces is really high between day 1 and day 3 of the culture time, so that the values for cell density at day 3 are similar to those found on the smooth surfaces and control surfaces at day 7. These results suggest that the patterned surfaces promote the cell adhesion and the subsequent cell proliferation. Interestingly, cell density attains maximal similar values on control cultures and the two material surfaces which reflect a confluent status of the culture on the three surfaces. The cell bridging between grooves can also contribute to the cell proliferation allowing an earlier cell confluence, highlighted by the significantly high growth rate observed between day 1 and day 3 on the patterned ceramic compared with control and the smooth ceramic.

Cell proliferation was also analysed by CLSM and SEM observations (Figs. 9 and 10).

At day 3, the presence of large cell clusters and areas without cells attest an heterogeneous repartition of the cells on the smooth surfaces (Fig. 9a) whereas homogeneous layers of cells are observed in the case of patterned surfaces (Fig. 9d). This result also indicates that the

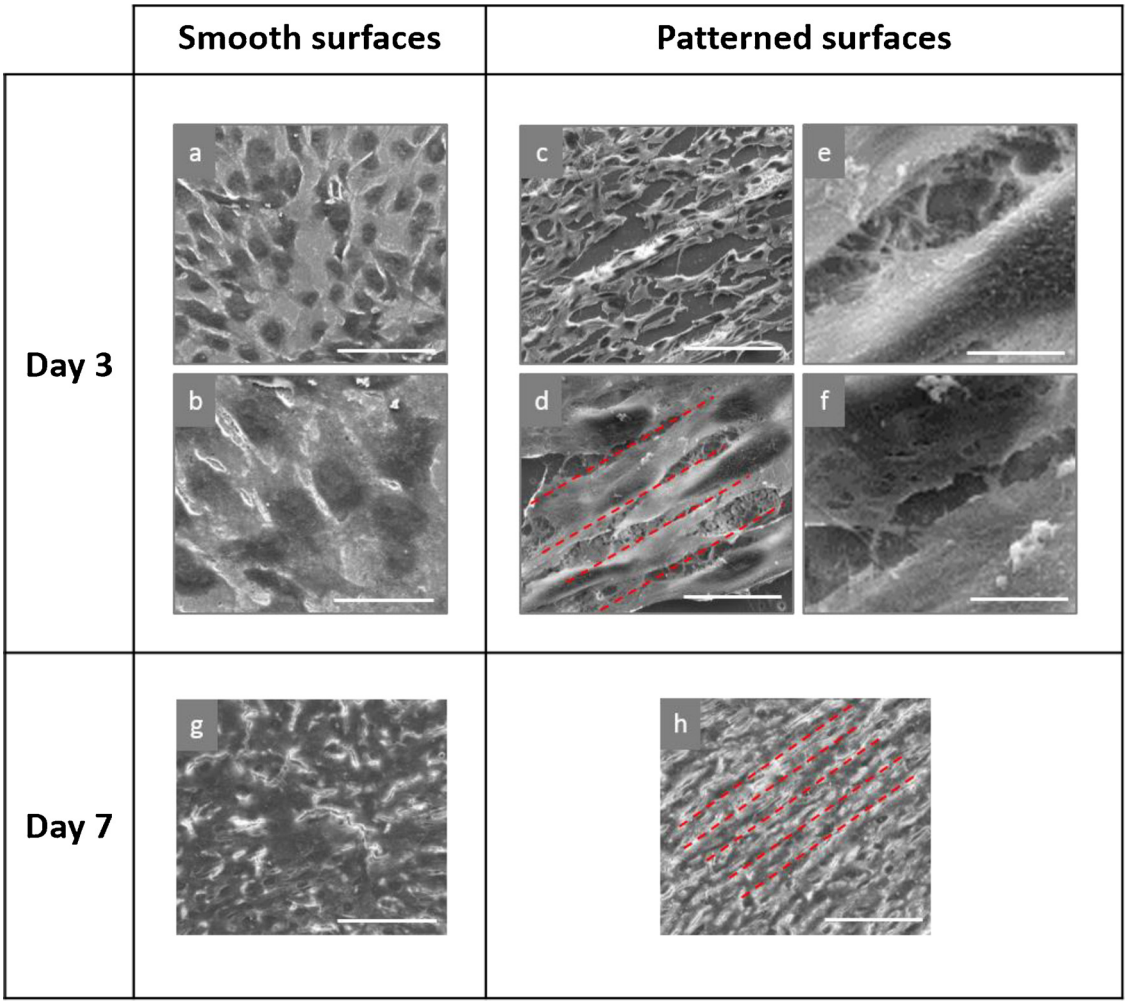


**Fig. 10.** SEM micrographs of MG63 osteoblastic cells adhering on sintered β-TCP substrates, three days and seven days after seeding: smooth surfaces (a, b, g) and patterned surfaces (c–f, h); scale bar: 100 µm (a, c, g, h), 20 µm (b, d) and 5 µm (e, f). Grooves direction is notified by the red lines. (For interpretation of the references to colour in this figure legend, the reader is referred to the web version of this article).

patterned topography seems to improve the cell colonisation, in line with the previous results. As the surface is partially covered in the case of the smooth surfaces, the cell population can still increase. Regarding the patterned surfaces, it is totally covered by the cells. Because of the cell layer confluence, cell growth is no longer observed, which is consistent with the quantitative resazurin results (Fig. 8). Observations at higher magnification confirm the alignment tendency of the cells already observed at day 1, for the patterned surfaces (Fig. 9e, f) compared to the smooth surfaces (Fig. 9b, c). This typical cell elongation behaviour has already been observed, for example, with fibroblast on PEG hydrogel surfaces with gold micro-stripes [35] and with MG63 in β-TCP macroporous structures [8].

After 3 days, the SEM micrographs show the same pattern of cell distribution over the two surfaces (Fig. 10). The smooth surfaces present randomly distributed cells (Fig. 10a, b) whereas the tendency of cell elongation along the grooves is still observable in the case of the patterned surfaces, not only inside the grooves, but even on the complete surface (Fig. 10c, d). In a high magnification, the close interaction of the cells within the groove rough topography as well as between adjacent aligned cells is well evidenced (Fig. 10e, f).

The SEM observations at day 7 (Fig. 10g, h) testify the presence of several cell layers. These observations confirm the growth slowing highlighted by the quantitative analyses attributed to the cells confluence (Fig. 8). Despite this accumulation of cellular layers, the orientation of the cells can be still clearly identified on the micrographs, in the case of the patterned surfaces, even on the top cellular layer (Fig. 10h). These observations show that the effect of the surface pattern is not limited at the first cell layer covering the surface.

Results of both MG63 cell proliferation and MG63 cell morphology studies performed in this work suggest that cell activity could be related with cell shape changes as it was especially the case for endothelial cells as shown in previous studies [36]. Indeed, it was well established that endothelial cell shape information are transduced into gene expression through mechanical forces transmitted by the cytoskeleton [37]. These results obtained in the present study on β-TCP micropatterned surfaces are therefore encouraging for the study of stem cells gene expression coupled to the morphological study of stem cells on such micro-patterned CaP substrates.

Moreover, the surface roughness can have a precise role in the proliferation and morphological phenomena observed in this work, as it has already been suggested in the literature that the surface roughness can have an effect on the profile of genes expressed by osteoblast cells [38].

## 4. Conclusion

In this study, linear micro-patterned β-TCP surfaces were produced by a femtosecond laser with several process parameters combinations, in order to investigate the heat affected zone generated by the laser irradiation. The micro-Raman analyses especially show a phase

transformation from β-TCP initial phase into α-TCP phase, strictly localised inside the grooves produced by the laser, highlighting a highly localised heating produced by the femtosecond laser irradiation. The first results suggest a possibility to reduce the thermal impact by optimisation of the process parameters. The XRD analyses, correlated with micro-Raman analyses, confirm that the use of femtosecond pulsed laser enables to limit the heat affected zone. Finally, the phase investigation inside the grooves, performed by micro-Raman spectroscopy, allowed to verify the optimised parameters to obtain β-TCP micro-patterned surfaces with continuous and well defined linear grooves, avoiding the allotropic transformation of β-TCP into α-TCP. This study show that micro-patterning of calcium phosphate surfaces by laser treatment is possible with the use of a short pulse width and an accurate control of the process parameters.

The contact angle measurements has shown an improvement of the wettability with the patterning compared to smooth surfaces. The improvement of the osteoblastic proliferation was also demonstrated with a high increase of MG63 population growth in presence of micro-patterning, highlighted by reaching the confluence significantly faster than on smooth substrates. Moreover, the tendency of cell elongation along the grooves direction in the case of linear patterned surfaces showed the ability of osteoblastic cells to adapt their morphology to the topography of the support on which they grow. Finally, the design of the patterned ceramic regarding the distance between grooves and the grooves features as roughness, depth and width result in a positive effect on cell growth. This appears to be fostered by the induction of the cell bridging between the grooves governed by the particular design of the material surface.

## Acknowledgements

The authors are grateful to the JECS Trust for funding the visit of Marie Lasgorceix to the Laboratory INEB (Contract N°2015106). Marie Lasgorceix also acknowledges the Walloon Region for financial support, within the “BEWARE” program (convention n°1510392) co-funded by Wallonia and European Union (FP7 – Marie Curie Actions). The authors are grateful to Dr Sylvain Desprez (Materia Nova, Mons, Belgium) for micro-Raman analyses. This publication is based on the work of COST Action MP1301, funded by COST (European Cooperation in Science and Technology) www.cost.eu.

## References

[1] M. Jarcho, Calcium phosphate ceramics as hard tissue prosthetics, Clin. Orthop. (1981) 259–278.
[2] S. Samavedi, A.R. Whittington, A.S. Goldstein, Calcium phosphate ceramics in bone tissue engineering: a review of properties and their influence on cell behavior, Acta Biomater. 9 (2013) 8037–8045, https://doi.org/10.1016/j.actbio.2013.06.014.
[3] I. Denry, L.T. Kuhn, Design and characterization of calcium phosphate ceramic scaffolds for bone tissue engineering, Dent. Mater. 32 (2016) 43–53, https://doi.org/10.1016/j.dental.2015.09.008.
[4] S.M. Best, A.E. Porter, E.S. Thian, J. Huang, Bioceramics: past, present and for the future, J. Eur. Ceram. Soc. 28 (2008) 1319–1327, https://doi.org/10.1016/j.jeurceramsoc.2007.12.001.
[5] M. Descamps, T. Duhoo, F. Monchau, J. Lu, P. Hardouin, J.-C. Hornez, A. Leriche, Manufacture of macroporous β-tricalcium phosphate bioceramics, J. Eur. Ceram. Soc. 28 (2008) 149–167, https://doi.org/10.1016/j.jeurceramsoc.2007.05.025.
[6] S. Deville, E. Saiz, A.P. Tomsia, Freeze casting of hydroxyapatite scaffolds for bone tissue engineering, Biomaterials 27 (2006) 5480–5489, https://doi.org/10.1016/j.biomaterials.2006.06.028.
[7] M. Lasgorceix, E. Champion, T. Chartier, Shaping by microstereolithography and sintering of macro–micro-porous silicon substituted hydroxyapatite, J. Eur. Ceram. Soc. 36 (2015) 1091–1101, https://doi.org/10.1016/j.jeurceramsoc.2015.11.020.
[8] E. Meurice, F. Bouchart, J.C. Hornez, A. Leriche, D. Hautcoeur, V. Lardot, F. Cambier, M.H. Fernandes, F. Monteiro, Osteoblastic cells colonization inside beta-TCP macroporous structures obtained by ice-templating, J. Eur. Ceram. Soc. 12 (2016) 2895–2901, https://doi.org/10.1016/j.jeurceramsoc.2015.10.030.
[9] A. Magnaudeix, J. Usseglio, M. Lasgorceix, F. Lalloue, C. Damia, J. Brie, P. Pascaud-Mathieu, E. Champion, Quantitative analysis of vascular colonisation and angio-conduction in porous silicon-substituted hydroxyapatite with various pore shapes in a chick chorioallantoic membrane (CAM) model, Acta Biomater. 38 (2016) 179–189, https://doi.org/10.1016/j.actbio.2016.04.039.
[10] C.M. Bidan, K.P. Kommareddy, M. Rumpler, P. Kollmannsberger, P. Fratzl, J.W.C. Dunlop, Geometry as a factor for tissue growth: towards shape optimization of tissue engineering scaffolds, Adv. Healthc. Mater. 2 (2013) 186–194, https://doi.org/10.1002/adhm.201200159.
[11] X. Yao, R. Peng, J. Ding, Cell-material interactions revealed via material techniques of surface patterning, Adv. Mater. Deerfield Beach Fla. 25 (2013) 5257–5286, https://doi.org/10.1002/adma.201301762.
[12] O. Zinger, G. Zhao, Z. Schwartz, J. Simpson, M. Wieland, D. Landolt, B. Boyan, Differential regulation of osteoblasts by substrate microstructural features, Biomaterials 26 (2005) 1837–1847, https://doi.org/10.1016/j.biomaterials.2004.06.035.
[13] M. Estévez, E. Martínez, S.J. Yarwood, M.J. Dalby, J. Samitier, Adhesion and migration of cells responding to microtopography, J. Biomed. Mater. Res. A 103 (2015) 1659–1668, https://doi.org/10.1002/jbm.a.35293.
[14] A.-M. Stanciuc, Q. Flamant, C.M. Sprecher, M. Alini, M. Anglada, M. Peroglio, Femtosecond laser multi-patterning of zirconia for screening of cell-surface interactions, J. Eur. Ceram. Soc. 38 (2018) 939–948, https://doi.org/10.1016/j.jeurceramsoc.2017.08.019.
[15] K. Zhang, Y. Fan, N. Dunne, X. Li, Effect of microporosity on scaffolds for bone tissue engineering, Regen. Biomater. (2018) 1–10, https://doi.org/10.1093/rb/rby001.
[16] C. Liang, H. Wang, J. Yang, B. Li, Y. Yang, H. Li, Biocompatibility of the micro-patterned NiTi surface produced by femtosecond laser, Appl. Surf. Sci. 261 (2012) 337–342, https://doi.org/10.1016/j.apsusc.2012.08.011.
[17] B. Li, M. Zhou, W. Zhang, G. Amoako, C. Gao, Comparison of structures and hydrophobicity of femtosecond and nanosecond laser-etched surfaces on silicon, Appl. Surf. Sci. 263 (2012) 45–49, https://doi.org/10.1016/j.apsusc.2012.08.092.
[18] Y.H. Jeong, I.B. Son, H.C. Choe, Formation of surface roughness on the Ti-35Nb-xZr alloy using femtosecond laser for biocompatibility, Procedia Eng. 10 (2011) 2393–2398, https://doi.org/10.1016/j.proeng.2011.04.394.
[19] A. Cunha, A.P. Serro, V. Oliveira, A. Almeida, R. Vilar, M.-C. Durrieu, Wetting behaviour of femtosecond laser textured Ti–6Al–4V surfaces, Appl. Surf. Sci. 265 (2013) 688–696, https://doi.org/10.1016/j.apsusc.2012.11.085.
[20] A. Cunha, A.-M. Elie, L. Plawinski, A.P. Serro, A.M. Botelho do Rego, A. Almeida, M.C. Urdaci, M.-C. Durrieu, R. Vilar, Femtosecond laser surface texturing of titanium as a method to reduce the adhesion of Staphylococcus aureus and biofilm formation, Appl. Surf. Sci. 360 (2016) 485–493, https://doi.org/10.1016/j.apsusc.2015.10.102.
[21] S. Raynaud, E. Champion, D. Bernache-Assollant, Calcium phosphate apatites with variable Ca/P atomic ratio II. Calcination and sintering, Biomaterials 23 (2002) 1073–1080, https://doi.org/10.1016/S0142-9612(01)00219-8.
[22] R.G. Carrodeguas, S. De Aza, α-Tricalcium phosphate: synthesis, properties and biomedical applications, Acta Biomater. 7 (2011) 3536–3546, https://doi.org/10.1016/j.actbio.2011.06.019.
[23] S. Nakamura, R. Otsuka, H. Aoki, M. Akao, N. Miura, T. Yamamoto, Thermal expansion of hydroxyapatite-β-tricalcium phosphate ceramics, Thermochim. Acta 165 (1990) 57–72, https://doi.org/10.1016/0040-6031(90)80206-E.
[24] M. Lasgorceix, C. Ott, L. Boilet, S. Hocquet, A. Leriche, M. Asadian, N. De Geyter, H. Declercq, V. Lardot, F. Cambier, Micropatterning of beta tricalcium phosphate bioceramic surfaces, by femtosecond laser, for bone marrow stemcells behavior assessment, Mater. Sci. Eng. C (2018), https://doi.org/10.1016/j.msec.2018.03.004.
[25] S. Raynaud, E. Champion, D. Bernache-Assollant, P. Thomas, Calcium phosphate apatites with variable Ca/P atomic ratio I. Synthesis, characterisation and thermal stability of powders, Biomaterials 23 (2002) 1065–1072, https://doi.org/10.1016/S0142-9612(01)00218-6.
[26] M. Descamps, O. Richart, P. Hardouin, J.C. Hornez, A. Leriche, Synthesis of macroporous β-tricalcium phosphate with controlled porous architectural, Ceram. Int. 34 (2008) 1131–1137, https://doi.org/10.1016/j.ceramint.2007.01.004.
[27] C. Rey, C. Combes, C. Drouet, D. Grossin, 1.111 – Bioactive ceramics: physical chemistry, in: P. Ducheyne (Ed.), Compr. Biomater. Elsevier, Oxford, 2011, pp. 187–221, , https://doi.org/10.1016/B978-0-08-055294-1.00178-1.
[28] A. Jillavenkatesa, R.A. Condrate Sr., The infrared and Raman spectra of β-and α-tricalcium phosphate (Ca3(PO4)2), Spectrosc. Lett. 31 (1998) 1619–1634, https://doi.org/10.1080/00387019808007439.
[29] G. Penel, N. Leroy, P. Van Landuyt, B. Flautre, P. Hardouin, J. Lemaître, G. Leroy, Raman microspectrometry studies of brushite cement: in vivo evolution in a sheep model, Bone 25 (1999) 81S–84S.
[30] M.M. Gentleman, E. Gentleman, The role of surface free energy in osteoblast–biomaterial interactions, Int. Mater. Rev. 59 (2014) 417–429, https://doi.org/10.1179/1743280414Y.0000000038.
[31] D. Quéré, Wetting and roughness, Annu. Rev. Mater. Res. 38 (2008) 71–99, https://doi.org/10.1146/annurev.matsci.38.060407.132434.
[32] J.Y. Chung, J.P. Youngblood, C.M. Stafford, Anisotropic wetting on tunable micro-wrinkled surfaces, Soft Matter 3 (2007) 1163–1169, https://doi.org/10.1039/B705112C.
[33] J.T. Parsons, A.R. Horwitz, M.A. Schwartz, Cell adhesion: integrating cytoskeletal dynamics and cellular tension, Nat. Rev. Mol. Cell Biol. 11 (2010) 633–643, https://doi.org/10.1038/nrm2957.
[34] L. Juignet, B. Charbonnier, V. Dumas, W. Bouleftour, M. Thomas, C. Laurent, L. Vico, N. Douard, D. Marchat, L. Malaval, Macrotopographic closure promotes tissue growth and osteogenesis in vitro, Acta Biomater. 53 (2017) 536–548, https://doi.org/10.1016/j.actbio.2017.02.037.
[35] J. Sun, J. Tang, J. Ding, Cell orientation on a stripe-micropatterned surface, Chin. Sci. Bull. 54 (2009) 3154–3159, https://doi.org/10.1007/s11434-009-0240-1.
[36] M. Versaevel, T. Grevesse, S. Gabriele, Spatial coordination between cell and nuclear shape within micropatterned endothelial cells, Nat. Commun. 3 (2012) 671, https://doi.org/10.1038/ncomms1668.
[37] A.J. Maniotis, C.S. Chen, D.E. Ingber, Demonstration of mechanical connections between integrins, cytoskeletal filaments, and nucleoplasm that stabilize nuclear structure, Proc. Natl. Acad. Sci. 94 (1997) 849–854.
[38] P.M. Brett, J. Harle, V. Salih, R. Mihoc, I. Olsen, F.H. Jones, M. Tonetti, Roughness response genes in osteoblasts, Bone 35 (2004) 124–133, https://doi.org/10.1016/j.bone.2004.03.009.